

SPATIO-TEMPORAL EVOLUTION OF HANLE AND ZEEMAN
SYNTHETIC POLARIZATION IN A CHROMOSPHERIC SPECTRAL LINE

E.S. CARLIN¹, BIANDA M.¹

ABSTRACT

Due to the quick evolution of the solar chromosphere, its magnetic field cannot be inferred reliably without accounting for the temporal variations of its polarized light. This has been broadly overlooked in the modelling and interpretation of the polarization due to technical problems (e.g., lack of temporal resolution or of time-dependent MHD solar models) and/or because many polarization measurements can apparently be explained without dynamics. Here, we show that the temporal evolution is critic for explaining the spectral-line scattering polarization because of its sensitivity to rapidly-varying physical quantities and the possibility of signal cancellations and attenuation during extended time integration. For studying the combined effect of time-varying magnetic fields and kinematics, we solved the 1.5D NLTE problem of the second kind in time-dependent 3D R-MHD solar models and we synthesized the Hanle and Zeeman polarization in forward scattering for the chromospheric $\lambda 4227$ line. We find that the quiet-sun polarization amplitudes depend on the periodicity and spectral coherence of the signal enhancements produced by kinematics, but that substantially larger linear polarization signals should exist all over the solar disk for short integration times. The spectral morphology of the polarization is discussed as a combination of Hanle, Zeeman, dynamic effects and partial redistribution. We give physical references for observations by degrading and characterizing our slit time-series in different spatio-temporal resolutions. The implications of our results for the interpretation of the second solar spectrum and for the investigation of the solar atmospheric heatings are discussed.

Keywords: Polarization — scattering — radiative transfer — shock waves — Sun: chromosphere — stars: atmospheres

1. INTRODUCTION

Two 4-m class solar telescopes (EST: Collados et al. (2013); and DKIST: Rimmele et al. (2013)) with exceptional spectropolarimetric capabilities are being developed at the present moment. They are expected to provide a sensitivity of 10^{-4} while preserving the spatio-temporal resolution of $\approx 0.''1 \times 20$ s required for following the evolution of the chromospheric spectral line polarization. Without it the signals end up being significantly integrated in space, time and/or wavelength, either intrinsically, by an instrument without enough resolution, or after detection, for increasing the S/N delivered by the spectropolarimeter.

Thus, spatiotemporal integration limits the study of the quiet solar chromosphere. Possible sign cancellations below the resolution element definitely kills the already faint transversal Zeeman signals produced by the weak chromospheric magnetism. The only alternative are then scattering signals, which can exist even in absence of magnetic field. Atoms scattering polarized light is the closest thing to an ideal in-situ detector of plasma properties (with data transponder incorporated), exhibiting large responsiveness to chromospheric magnetic fields by Hanle effect, but also to the chromospheric temperature and velocity gradients via changes in radiation field anisotropy and atomic polarization (Carlin et al. 2012, 2013). Anisotropic radiation also adds sensitivity to the horizontal inhomogeneities in the plasma when the three-dimensional structure of the radiation field is considered (Štěpán et al. 2015; Tichý et al. 2015). When by this or other reason the symmetry in the scattering is broken

(e.g., by a non-radial magnetic field in forward scattering), the modulation of chromospheric atomic polarization produced by shock waves becomes visible in large and frequent changes in the shape, sign and amplitude of the emergent profiles (Carlin & Asensio Ramos 2015). Thus, it has been recently pointed out that in contrast with previous expectations sign cancellations can also affect the Hanle polarization signatures for current typical resolutions (Carlin & Bianda 2016, hereafter the Letter).

Note that the current maximum *spatial* resolution seems enough for tracking spatial variations of the quiet chromospheric magnetism through scattering Hanle signals (which is yet harder with the transversal Zeeman effect). However, the temporal scales of the chromosphere are significantly shorter than the several minutes that most observations of scattering polarization last. Hence, analyzing a time average the information contained in the temporal evolution -e.g. continuity and causality of events- is lost, and the comparison with calculations becomes misleading. Furthermore, as chromospheric events can be very fast, they are not statistically well represented in calculations with single MHD snapshots of limited extension. For target resolutions around $0.''1 \times 20$ s, our calculations support detection of *near ubiquitous* scattering polarization signals in the quiet chromosphere once a sensitivity of 10^{-4} (10^{-3} for some spectral lines) is surpassed. This threshold is quiet particular. Its crossing is a sort of discrete leap that should allow the detection of the faint disk-center quiet sun polarization, thus obtaining an almost fully polarized solar disk in several spectral lines, something to expect with the coming generation of solar facilities. Thus, our simulations try to estimate the polarization that a 4-m class solar telescope might ob-

escarlin@irsol.es

¹ Istituto Ricerche Solari Locarno, 6600, Locarno, Switzerland

serve when the dynamic signals are measured in their proper time scales. On the other hand, we expect that this work help to find a way of disentangling the effect of velocities and magnetic fields in the Hanle signals of chromospheric lines. Our recent Letter advanced some of the results, pointing out that a minimal understanding of the temporal evolution of the polarization is required for determining magnetic fields in dynamic layers as well as for deciphering the second solar spectrum.

In the present paper we continue studying the Stokes signals of the $\lambda 4227$ line (located at 4226.728 \AA in air). This paradigmatic spectral line of the second solar spectrum has been widely studied, both observationally and theoretically, in the last 50 years. Some examples are Brückner (1963), Dumont et al. (1973), Stenflo (1974), Dumont et al. (1977), Faurobert-Scholl (1992), Bianda et al. (1998), Holzreuter et al. (2005), Sampoorna et al. (2009), Anusha et al. (2010), Bianda et al. (2011) or Supriya et al. (2014). We improve upon these studies by using a time-series of realistic 3D radiation-MHD models as input atmospheres, and by studying the effect of spatio-temporal integration and dynamics on the Hanle and Zeeman signals in the whole Stokes vector. We call Ca I 4227 \AA a *reference line* because the quantification of dynamic effects in its spectral core gives useful physical insights for unpuzzling other scattering signals forming at similar heights but with richer atomic structure, such as the Na I D lines. $\lambda 4227$ seems indeed ideal for this purpose because it is a chromospheric spectral line with minimal quantum complexity: normal Zeeman triplet, no hyperfine structure, no lower level polarization. Furthermore, its large forward-scattering polarization signals in all Stokes parameters permits to explore the lower chromosphere at and around disk center, which avoids the more complex interpretation of line-of-sight superposition effects at the solar limb (see introduction of Carlin 2015).

After presenting our results (Sec. 3), we present some discussions (sec. 4). The key in Sec. 4 is that the degeneracy in the solar signals can lead to close fits with simulations implying, however, wrong physical inferences; and that this is avoided with larger spatio-temporal resolutions and a precise characterization of the effect of chromospheric dynamics (i.e., time evolution of macroscopic motions and heatings) in the polarization.

2. SYNTHESIS OF THE POLARIZATION SIGNALS

2.1. The atmospheric model

The input for our calculations is a time-dependent MHD simulation computed with the Bifrost code (Gudiksen et al. 2011) considering non-equilibrium hydrogen ionization. It emulates a bipolar magnetic structure with network properties and its quiet sun surroundings, having an average unsigned magnetic field strength of 48 G in the model photosphere. The spatial physical domain covers a horizontal extension of $24 \times 24 \text{ Mm}^2$ with a horizontal resolution of 48 km and a vertical resolution of 19 km in photosphere and chromosphere. The temporal evolution lasts 15 minutes of solar time with a resolution of 10 seconds. For more details see Carlsson et al. (2016). Figure 1 shows the slit-like region of $\approx 0.''5 \times 33''$ (it has a certain width) that was selected in the models for our calculations.

2.2. Calculation procedure

We developed a pipeline of programs that processes data levels in independent steps. In the step 1 the MHD simulation (data level 1) is read and transformed for multidimensional visualization and plotting (data level 2). Having selected the region where the radiative transfer is to be carried out, the inputs (data level 3) for the RH 1.5D code (Pereira & Uitenbroek 2015; Uitenbroek 2001) are created. Such code is set to solve the NLTE ionization balance between Ca I and Ca II using a 20-level atomic model that accounts for the lower transitions of Ca I and the ground level of Ca II with 19 continuum transitions and 17 line transitions. Photoionization and inelastic collisional excitations/de-excitations due to electrons are considered for all levels. The inclusion of Ca III is negligible for computing the Ca I populations because the population of the former starts to be significant from heights above the upper chromosphere, while Ca I forms entirely below the middle chromosphere. Thus, in the solar models considered, Ca II provides all the reservoir population.

The calculation of atomic populations with RH was done considering partial redistribution (Leenaarts et al. 2012). Comparing the results in PRD and CRD we have seen that this affects (not dramatically) the atomic populations. The reason is simply that the NLTE mean radiation field is slightly affected by the increased PRD emissivity.

The atomic populations resulting for the levels of the $\lambda 4227$ line and the MHD quantities are the input (data level 4) for Handy' (HANle DYnamic Polarized Radiation In Moving Envelopes). This code solves the non-LTE radiative transfer problem of the second kind (Landi Degl'Innocenti & Landolfi 2004, sec.14.1; LL04 hereafter) processing each time-step independently and applying the 1.5D (or column-by-column) approximation to each pixel of the slit. Thus, horizontal inhomogeneities and horizontal velocity gradients do not contribute to the non-local part of the problem (the radiation field). The non-LTE iteration provides the converged values of the the components of the statistical density matrix, which accounts for atomic populations, atomic polarization and quantum coherences in magnetic energy sub-levels. The emergent radiative transfer performed from the converged atomic density matrix is fully realistic in forward-scattering (disk center line of sight). The local physics (collisions, Zeeman and Hanle effects) is properly treated. This approach allows to investigate the effect of vertical variations in the MHD quantities and provides of spatio-temporal continuity to the results.

The calculations with polarization were done in the regime of complete redistribution (CRD). This is justified because, though spectral PRD wings are increasingly generated for decreasing μ values, partial redistribution does not affect the line core profiles at disk-center, meaning a range of $\mu = [0.89, 1]$ for the $\lambda 4227$ line (e.g., Dumont et al. 1973; Anusha et al. 2011). Our results point out that this is true in a more restricted disk center area, roughly for $\mu \in [0.96, 1]$, but for smaller μ values the combination of chromospheric velocities and photospheric velocity drifts with lack of time resolution can make that the line core linear polarization (LP) and the near-core PRD wings overlap in wavelength (see Letter or Sec.3.8).

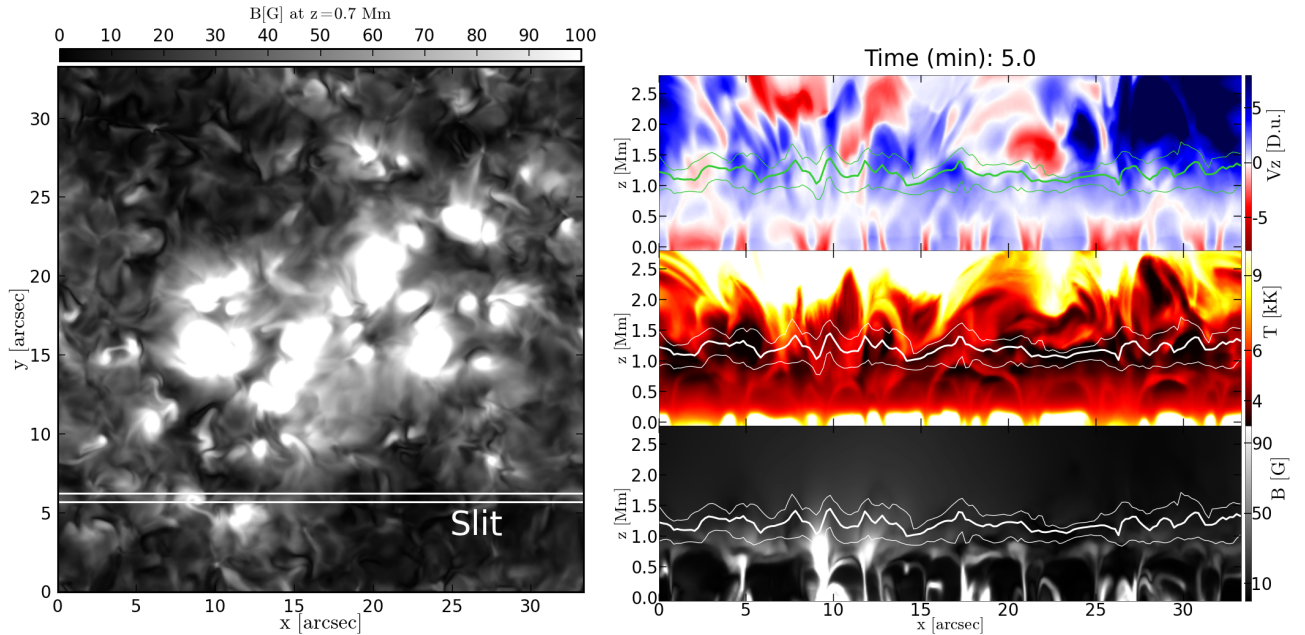


Figure 1. Left: magnetic field strength saturated in 100 G at $z=0.7$ Mm. Right: the formation heights of Ca I 4227 Å line samples the low chromosphere above the small-scale magnetic canopy. The thin white lines mark the formation region $\tau \in [0.1, 10]$ for the wavelength of the intensity minimum. The thicker white line marks $\tau = 1$.

In any case, the $\lambda 4227$ line core is not blended or affected by the weak spectral lines forming in its proximities (Lites 1974). Continuum polarization is generally very small and is also minimized in forward-scattering.

For this paper the pure Zeeman effect (no atomic polarization, no quantum coherences) in Q, U and V was calculated separately from the Hanle signals in order to compare both contributions to the LP. Namely the equations solved here are: the statistical equilibrium equations given by a suitable combination of Eqs. (7.2.a) and Eq. (7.101) of LL04 under the impact approximation and the assumption of isotropy for depolarizing and inelastic collisions (Lamb & Ter Haar 1971); and the radiative transfer equation for an instantaneously-stationary radiation field with propagation matrix given by Eqs. 7.2.b (Hanle regime) and by Eqs. (9.4), (9.7) and (9.10) (Zeeman regime) of LL04 neglecting stimulated emission. The optical profiles entering in the propagation matrix are calculated using a damping parameter that includes the dominant contributions of radiative ($A_{ul} = 2.18 \cdot 10^8$) and Van der Waals ($\gamma_{v_{dW}} = 1.7 \cdot 10^{-8}$, $a_{v_{dW}} = 0.389$) broadening (Faurobert-Scholl 1992; Stenflo 1974). The resolution of the wavelength and angular grids are automatically set by adapting them to the level of kinematics affecting the radiative transfer. When integrating in angle (e.g., to obtain the radiation field tensor) we use a gaussian quadrature whose minimal number of points in inclination angles is defined by the rule explained in Fig.2.

The final step of the calculations tries to facilitate the analysis. It involves the characterization of the Stokes signals and of the physical quantities related to polarization at the region of formation of each wavelength. These metrics (data level 5) allow us to correlate detailed quantities in multiple dimensions for understanding possible patterns that can lead to better diagnosis in time-dependent atmospheres. All data levels are structured

following NetCDF4 standards². All our calculations were done for microturbulent velocity $v_{\text{micro}} = 0 \text{ km s}^{-1}$ and $v_{\text{micro}} = 2 \text{ km s}^{-1}$.

2.3. Minor modifications to RH 1.5D

In presence of shock waves the numerical convergence of some radiative transfer codes with polarization is usually not guaranteed because a mere Doppler shift can make the elements of the propagation matrix of consecutive points in the optical path to differ abruptly in amplitude at a given wavelength. Physically, this is an obstacle specially in the low chromosphere. On one hand, because there the ratio between the vertical velocity gradients and the thermal broadening is usually larger than at other heights (by combination of shock waves and cool plasma pockets). On the other hand, because in the low chromosphere the frequent meeting between upward shocks and plasma falling back fast from previous waves produces larger velocity gradients. Numerically, the problem is that some formal solvers of the radiative transfer equation become unstable in such situations unless a very fine grid is used. Instead of modifying the formal solver used by RH we have assured stability and convergence modifying RH 1.5D for *redistributing*, when necessary, the atmospheric grid points towards those heights where certain proxies to opacity change more abruptly. Combining this method³ with an eventual better grid resolution all columns converge.

Other minor modifications done to RH for developing this work include: i) calculation of heights of formation for all wavelengths at additional optical depths in the transition of interest; ii) possibility of redefining the cutting atmospheric points using optical depth and hydrogen density thresholds respectively; iii) possibility of increasing the number of spatial grid points in run time.

² <http://www.unidata.ucar.edu/software/netcdf/>

³ To be eventually published in a separate publication.

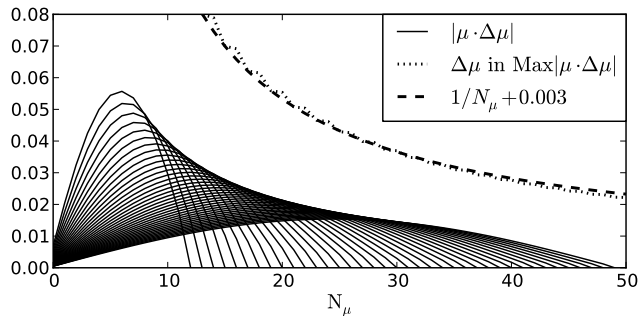


Figure 2. In presence of large vertical velocities the error in the gaussian quadratures used to calculate the radiation field tensor is larger for those rays whose $\xi = |\mu \cdot \Delta\mu|$ is maximum (with $\mu = \cos(\theta_k)$, and $\Delta\mu = \mu_{k+1} - \mu_k$, for a ray k). Continuous curves above show this quantity for different quadrature grids with number of points labelled by their cut with the horizontal axis. In order to give a rule for the number of angular points N_μ to be used, we take the $\Delta\mu$ at that maximum ξ as the limiting worst case. We find that such $\Delta\mu$ is $\approx 1/N_\mu + 0.003$ for any number of points. On the other hand, as $\Delta\mu$ must be $< 1/V_z^{\text{Max}}$ (V_z^{Max} being the maximum Doppler velocity in the atmosphere), the recipe turns out to be $N_\mu \gtrsim 2.1 \cdot V_z^{\text{Max}}$. This rule is only applied when giving a number larger than a safe minimum of 13 points per quadrant in inclination.

3. RESULTS

3.1. Magnetic references in semi-empirical models.

Before considering MHD models we calculated the emergent forward-scattering polarization in a FALC model (Fontenla et al. 1993) with a constant ad-hoc magnetic field. We did it for all possible magnetic field azimuths and inclinations, and for strengths between 10 and 130 G (Hanle saturation for Ca I $\lambda 4227$ every 10 G. Representing in the Poincaré sphere (Q,U,V space) the amplitude of each polarization profile for each case, we obtain an extension of a Hanle diagram, what we call a Poincaré diagram (Fig. 3). This representation has not been used before for characterizing the Hanle and Zeeman effects in a solar atmosphere, but it seems quiet advantageous to this regard. The additional Stokes V dimension in Poincaré diagrams partially breaks the degeneracy of polarization with magnetic field orientation. This representation gives a more compact and clear view of the limiting polarization values for a given spectral line and line of sight.

We find that at disk center the total LP of $\lambda 4227$ in semiempirical models is always in the range 0.1 – 0.5% for any magnetic field inclination $\theta_B \in [17^\circ, 163^\circ]$ and any azimuth if the magnetic field is lower than 50 G. Most magnetic fields affecting the line core in the time-dependent simulations are between this value and 10 G, hence very close to the optimal value that maximizes the Hanle effect and that is given by the upper-level Hanle critical field of 20 – 25 G.

As shown by Fig. 3, the previous minimum of LP=0.1%, given by near-vertical magnetic fields, is also produced at Van-Vleck inclinations: $\theta_B = [54.73^\circ, 125.27^\circ]$. Therefore, predominantly horizontal fields, with inclinations contained between those Van Vleck angles, cannot make Q/I, U/I and V/I to be below 0.1% in large areas simultaneously. If this happens observing a line whose S/N is expected to be good, we assume that is because collisions and/or dynamic effects are cancelling the polarization. In particular, a total LP < 0.1% over large solar areas suggests that dynamics

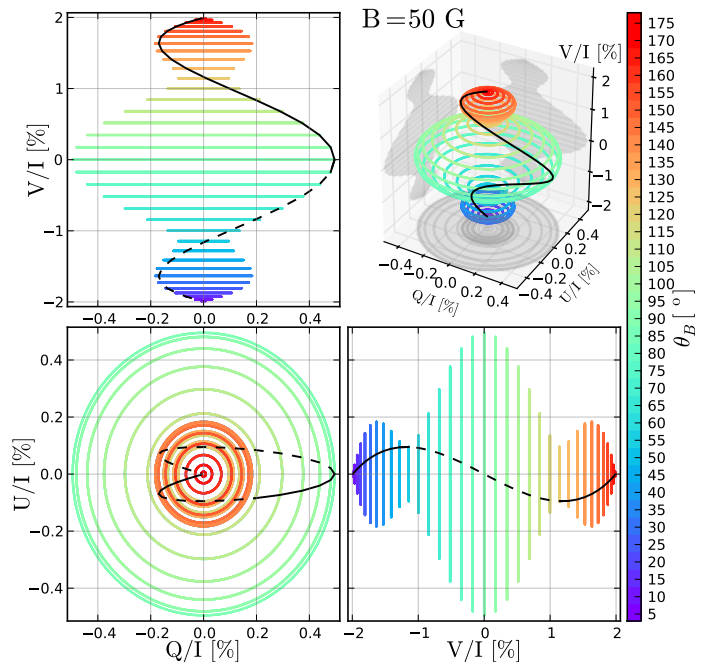


Figure 3. Poincaré diagram for: Ca I $\lambda 4227$, $\mu = 1$, FALC atmosphere, constant ad-hoc $B = 50$ G. The black line connects all points with $\chi_B - \chi = 90^\circ$ (χ sets the direction of $Q > 0$ in space).

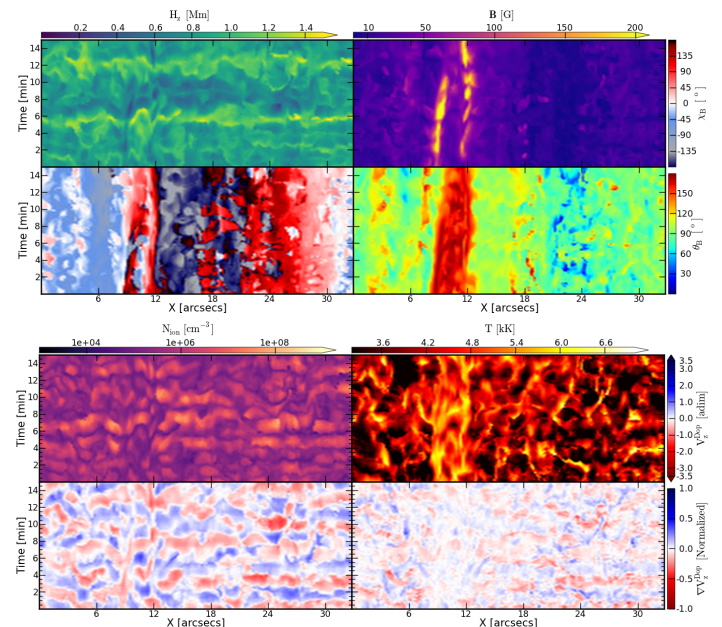


Figure 4. MHD quantities at $\tau = 1$ for the line-center wavelength in each timestep and length coordinate in the slit. Velocity shocks are here exposed by removing at each timestep the average offset velocity due to the 5-minute oscillations (see its effect in the height of formation). The vertical velocity map is on the left.

might be producing sign cancellations below the temporal resolution element (we will discuss this later). Here *dynamics* also refers to situations with a time-varying magnetic field in the resolution element. For instance, our simulations show that emerging cool bubbles seem to make the magnetic field inclination to oscillate between the horizontal and near-Van-Vleck angles (see Fig. 4 around $x = 18''$ and $x = 23''$).

If the maximum values of the measured LP are above

the semi-empirical (static) reference of 0.5%, it is necessary to assume that the amplifications introduced by macroscopic motions along time are significant, occurring at certain wavelengths with enough persistence (spectral coherence) and/or strength during the exposure time.

3.2. Formation region

Significant variations in the height of formation are normal in chromospheric lines. In the models considered the region of formation ($0.1 < \tau < 10$) of the minimum line-core intensity of $\lambda 4227$ oscillates between $0.7 < z < 1.5$ Mm, tending to contain the coolest atmospheric patches located just above the small-scale magnetic canopy (see Fig. 1, right panel). A first reason for this is that neutral Calcium density peaks in cool volumes. A second one is that in forward-scattering the height of formation is the lowest possible. Due to the proximity to the small-scale magnetic canopy, the region of $\tau = 1$ at the line core is normally filled by near-horizontal magnetic fields at any time, which maximizes the forward-scattering Hanle effect. Such magnetic canopy separates photosphere and chromosphere (see Fig. 1) and seems to play a role in the heating of the chromosphere (e.g., Goodman 1996). Also in these layers the incipient shock waves start to act significantly in the line core. In semiempirical models this corresponds to heights between the temperature minimum and the first temperature bump. A similar scenario is expected for chromospheric polarization signals of other neutral atomic elements.

3.3. Instantaneous polarization features

The temporal variations of the synthetic polarization profiles along the slit are large. The LP has almost-ubiquitous, sudden and conspicuous increments (in absolute value) moving rapidly along the spatial direction. An inspection of the instantaneous slit profiles in the temporal serie (e.g., in Letter, Fig. 5 in this paper, or Fig. 3 in Carlin 2016) reveals:

- the spatial exclusion (or complementarity) of linear and circular polarization due to their different sensitivities to transversal and longitudinal magnetic fields. An additional reason is that the formation region, though corrugated, is roughly parallel to the surface, hence crossing suddenly the vertical magnetic lines emerging from magnetic patches. In observations at disk-center, sizable V/I and line-core LP are sometimes co-spatial.
- a weak (negligible) transversal Zeeman effect along the whole slit, though $\lambda 4227$ forms in the low chromosphere. Hence, all relevant features in Q and U are Hanle polarization. As the field is relatively weak, the Zeeman profiles only have σ components. They usually enclose the spectral Hanle core, but sometimes they lay in it due to height-dependent longitudinal motions (see Fig.5). Each σ component is narrow (even with microturbulence) and can be, each of them, antisymmetric, so having opposite signs in their small spectral width. When this happens the variable Doppler shifts existing during the time integration can easily weaken the final LP Zeeman amplitudes.

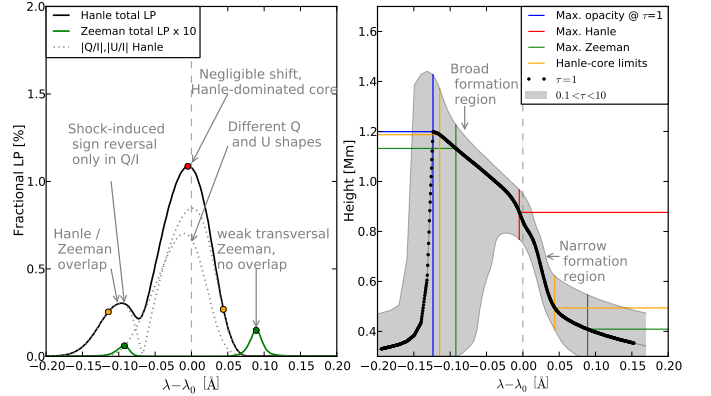


Figure 5. Typical Hanle and Zeeman signals (left) and formation region (right) for one pixel and timestep. Total LP is defined as $\sqrt{Q^2 + U^2}/I$. The Zeeman signals are multiplied by 10. The yellow dots and lines mark 30% of the Hanle maximum. Most of the LP features labelled in the figure change with time and pixel.

- the correlation between spectrally-broad strong circular polarization, heating signatures in intensity and stronger vertical magnetic fields. Spectrally-broad V/I profiles can be understood as a consequence of the weak-field approximation for Stokes V (being proportional to the wavelength derivative of the intensity) when the intensity profile has conspicuous peaks aside of the core and the longitudinal magnetic field is strong enough. At disk center, the formation region of the $\lambda 4227$ near-core peaks in intensity is already sub-chromospheric, hence the heatings creating such intensity excesses are not due to compressing shock waves.
- the dynamic modulation of Hanle signals by vertical gradients of velocity. The general response of the scattering LP signals to velocity gradients does not require lower level alignment (as did for Ca II IR triplet lines in Carlin et al. 2013) if the upper level can instead harbour it.
- the strong instantaneous amplitudes of the forward-scattering $\lambda 4227$ polarization. They are larger than in observations presumably because are calculated with spatial and temporal resolution, which minimizes cancellations. This should mean that magnetic field diagnosis via Hanle in the bulk of the chromosphere is not physically limited by too weak signals at disk center.
- the presence of antisymmetric LP profiles, without dominant sign (see Figs. 2 and 3 of Letter or Fig. 6). Hence, the Hanle core can in principle have any shape, and not necessarily a single line-core lobe as usually thought. The origins of such antisymmetric LP profiles are: a variation of magnetic field azimuth along the line of sight (LOS); and/or the modulation of the height-dependent radiation field anisotropy by vertical velocity gradients.
- the different instantaneous shapes of Q/I and U/I at a given same location. Due to the physical symmetry at disk center in 1.5D, one would expect Q/I and U/I with similar (normalized) shapes. This fails because the magnetic field azimuth changes

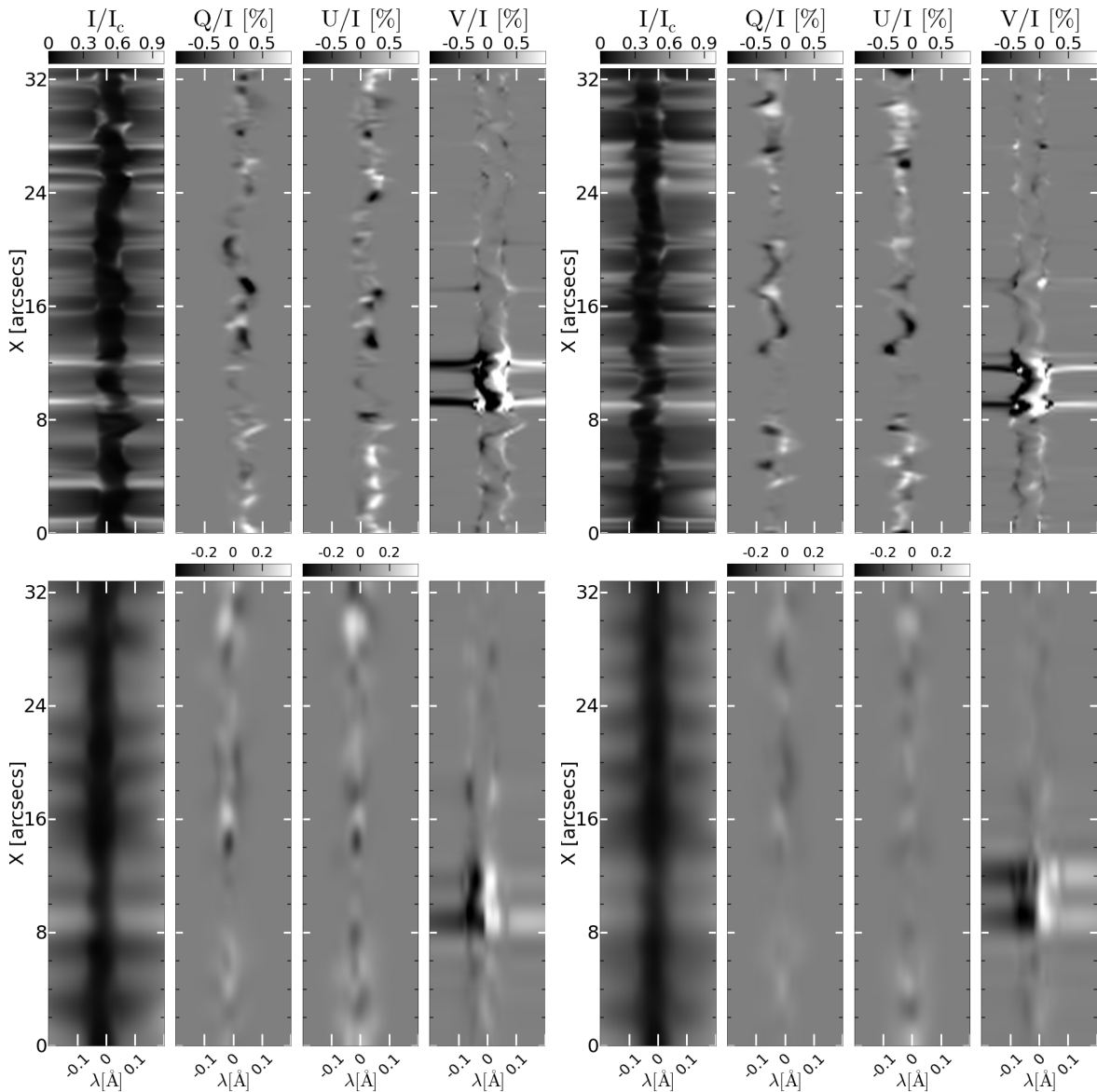


Figure 6. Slit profiles for $v_{\text{micro}} = 0 \text{ km s}^{-1}$. Upper panels: instantaneous signals in minimum (left) and maximum (right, 150 s later) of the supergranular convection. For calculating these panels we integrated each individual Stokes component in an area of 0.5 (slit width) $\times 0.2 \text{ arcsec}^2$. Lower panels: same as before but integrating 1.4 arcsec along the slit and 5 min (left panels) or 15 min (right panels) in time. LP is saturated to $\pm 1\%$ or $\pm 0.4\%$ as shown by the corresponding bars above each panel.

along $0.1 < \tau_\lambda < 10$, so that the height maximizing Q/I (i.e., where $\chi_B = 0, \pm 90, 180$) in a wavelength λ is different than in U/I (peaking in $\chi_B = \pm 45, \pm 135$). Thus, the magnetic field can narrow down the formation region of the polarization to specific layers. This also means that the difference in shape between both normalized profiles quantifies the magnetic field *azimuth gradient* along the LOS.

3.4. Polarization without microturbulence

Large scale photospheric oscillations introduce an offset Doppler shift with a period of 5 minutes that simultaneously affect all spectra along the slit. Comparing signals calculated without ad-hoc microturbulent velocity (see Fig. 6) in opposite instants in which the maximum 5-minutes-period Doppler shifts are maximum, it is seen that such shifts are larger than half the broadening of

the LP profile. When the chromospheric Doppler shifts (e.g., due to shock waves) are added, the result is LP profiles with reduced overlapping along time (compare upper LP panels of Fig. 6). This weakens and shapes the integrated LP signals due to their lack of reinforcement during the exposure time. Thus, integrating $1.4''$ and several minutes (5 and 15 min in lower left and right panels, respectively) we find synthetic LP signals that are weaker than those in the observations of Fig. 9. The maximum absolute LP value in the 15-min integration is 0.11% , which is four times weaker than in the observations with $v_{\text{micro}} = 2 \text{ km s}^{-1}$. Let us note that a distinctive point of the observed scattering polarization is to have significant amplitudes after long exposures, hence it is important to emulate this. Furthermore, without microturbulence all the Stokes components are too narrow.

3.5. Polarization with microturbulence

The observational constraints in broadening and amplitudes mentioned before are reasonably achieved when $v_{\text{micro}} = 2 \text{ km s}^{-1}$ (see Fig. 7). The significant improvement provided by the microturbulence points out that the lower chromosphere of the models is too cool (particularly around the coolest locations, where this line tends to form). The agreement in morphology is now also remarkable. A chain of near-symmetric LP rings⁴ appear after 5 min of integration, when the maximum integrated amplitudes coincide with the observed ones. Such an agreement between the left two panels of Fig. 7 and the observations results of adding up hundreds of very different instantaneous Stokes profiles (those in a bin of $1.4''$ and 5 minutes).

An equivalent example for longer exposure times (15 min) is given by the second pair of panels in the same figure. The maximum amplitudes are yet close to the observed ones, as required in Sec. 3.4. Additionally, there is attenuation over significant extensions of the slits, with amplitudes well below the minimum reference defined in semiempirical models in Sec. 3.1. This can help to explain the “noise pools” found in observations of scattering polarization. For instance, the very small (noisy) V/I, Q/I and U/I over the lowest part of the slit in the observation of Fig. 9 is surely not produced by a particular magnetic field orientation⁵ or by collisional processes, which should act in other close IN regions as well. Hence, dynamics might be the reason. Middle panels of Fig. 10 shows how dynamics and time integration attenuate up to a factor 20 our synthetic observations in relation to the maximum time-resolved signal in the same panels. Comparing with other locations of the slit with less attenuation we found that strong reductions are produced when the temporal evolution of the signals loose periodicity after a certain time, such that the pattern is not reinforced over long temporal scales. For instance, this happens where LP rings appear.

As in the observations, the V/I profile with microturbulence has a central spectral gap with near-zero amplitude when magnetic fields are vertical. The maximum V/I amplitudes suggests that the temporal scales are correct for the quantities and heights creating circular polarization. Averaging the two peaks of the profiles we find $[2.16 - (-1.85)]/2 \approx 2\%$ and $[0.84 - (-0.82)]/2 \approx 0.83\%$ (for the first and fifth strong V/I patch in Fig. 6) versus $[0.96 - (-0.84)]/2 = 0.9\%$ (for our 15-min-integration synthetic signals) This agreement is remarkable because the instantaneous V/I profiles are completely different than the integrated ones (see lowest rightmost panel in Fig. 10), which would apply to real observations though being usually not considered in the literature using the longitudinal Zeeman effect. This implies that longitudinal magnetic fields inferred from quiet sun observations without temporal resolution might be significantly weaker than the true ones.

As the calculations with $v_{\text{micro}} = 2 \text{ km s}^{-1}$ seem to rep-

⁴ These LP features resemble rings in the wavelength-space plane because the core Hanle signal is surrounded in space and wavelength by nearly symmetric peaks of opposite sign.

⁵ As shown in Sec. 3 with Poincaré diagrams, a Van-Vleck magnetic field inclination over the whole area and during the whole exposure time is quiet unlikely.

resent better the sun, only this case is considered in the following.

3.6. Emulating a longer slit

By repeating blocks of intensity and LP profiles (Q/I and U/I indistinctly) along space, Fig. 8 emulates a slit with the same length as in our observations. Second panel shows the synthetic intensity integrated over the 15 minutes. Stokes I/I_c has intensity variations (strips) along the spatial direction whose small scales are compatible with the observed 30-min average intensity in Fig. 9. In this latter figure one has to zoom a bit to see the less-contrasted strips (obtaining synthetic intensity strips with a similar low contrast is just a matter of adding the effect of the stray light in the telescope). The intensity strips are more evident toward the wings and seem to be due to sound waves altering temperature. In the simulations, they have more variability and contrast in weakly magnetized patches of the IN because there the plasma alternate periodically between lower and larger temperatures, which increases emissivity and modulates the damping parameter shaping the near-core. The synthetic intensity strips tend to disappear with stronger magnetic field, which correlates with reduced temperature and reduced vertical gradients of velocity. This suggests a relation between more active short-scale dynamics and LP rings. Zooming in the intensity in Fig. 9, we effectively have the impression that there is a certain correlation between the strips and the presence of LP rings in Q/I or U/I.

On the other hand, right-most panel of 8 shows that the synthetic LP (Q/I and U/I repeated in space) integrated over the 15-min serie is spatially different than in the 30-min observations in Fig. 9.

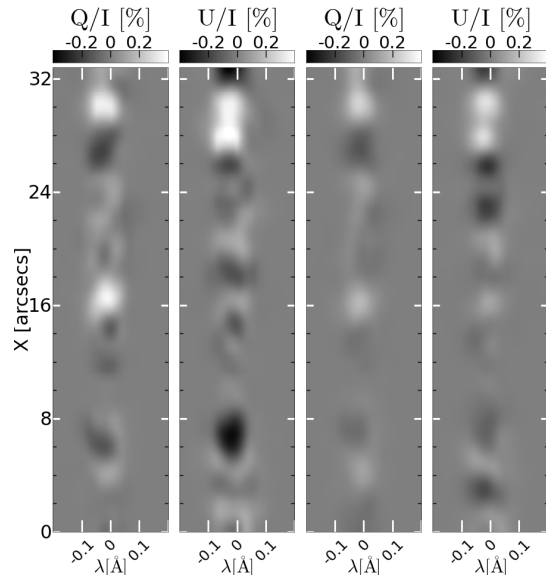


Figure 7. Unresolved LP with $v_{\text{micro}} = 2 \text{ km s}^{-1}$ and spatial resolution of 1.4 arcsecs. First two panels: LP after 5-min integration. Last two panels: LP after 15-min integration. The action of microturbulence allows to have measurable amplitudes after long exposures.

For shorter integration times, the spatial lengths of the synthetic LP rings are at least a factor 4 smaller than in

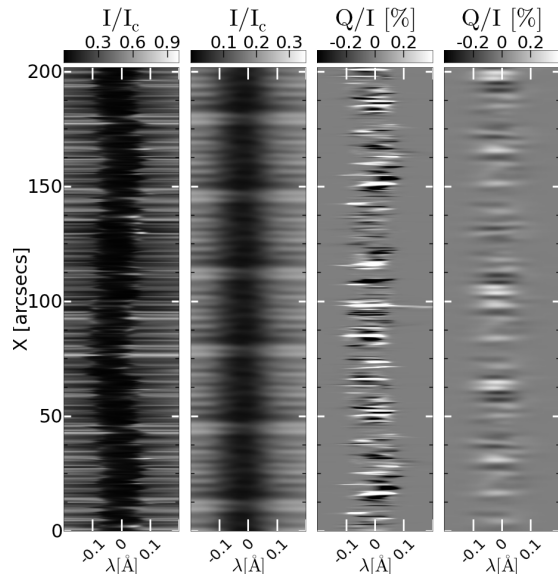


Figure 8. Spatial pile of synthetic profiles filling the length of the observational slit. First two panels: Intensity profiles with full spatio-temporal resolution and after integrating 15 min. Last two panels: same for Q/I. Actually, to avoid repetition the instantaneous panels were composed piling several slits of different timesteps while the averaged slits were obtained by mere repetition along space of the average profiles. Similarly, the average Q/I panel is a pile of Q/I and U/I average slits.

observations. The integration time needed for reproducing their line-core amplitudes is also significantly smaller (5-min) than the 30-min of the observations. In the Letter we tried to explain these differences in terms of: i) the combination of Hanle effect, kinematics, and lack of resolution, which are effects contained in our simulations; ii) transversal Zeeman effect, which shows negligible contribution in our simulations; and iii) partial redistribution effects (PRD), not considered by our calculations because in forward-scattering it plays no role, but possibly affecting the observations that were not taken exactly at $\mu = 1$. These factors behave differently in the two parts of the LP rings (the core and the near-core sign reversals surrounding it), hence they contribute differently to explain both parts. We will now present additional information that can help to clarify the reason of the differences in scale, starting by the contribution of the line core.

3.7. On the core of the linear polarization rings

The length of the LP rings is set by the spatial change of sign in the very line core. If the change was more frequent in space, the number of rings in the slit would be larger and their scale shorter. The maximum possible amplitudes of the synthetic and solar LP rings can be large (compared to the maximum reference values of semi-empirical models, see Sec. 3.1) and occurs at line center, not in the sign reversals.

In observations, the LP rings are interconnected by single-lobe signals (forming a chain of rings in IN areas). Similar structures appear in our simulations close to the intermittent emergence of photospheric magnetic elements that are associated with small-scale oscillating chromospheric fields. Figure 4 shows this at the level of the chromosphere. There, a regular emergence of cool plasma bubbles (see temperature panel around $x = 17''$ and $x = 22''$ between 0 and 8 min) develops into more pe-

riodic chromospheric shocks at stable locations. When seen in space-time diagrams, the temperature in these locations show post-shock rarefaction volumes, i.e. cool bubbles, that are periodic and look more rounded. The magnetic field inclination, azimuth and strength oscillate at such positions. The inclination oscillates between horizontal and near-Van-Vleck angles exposing opposite polarities for $x = 17''$ and $x = 22''$ in Fig. 4. In between those locations, the chromospheric magnetic field is always close to horizontal. The single-lobe signals linking the LP rings vary in location around such middle locations after integrating in time (Fig. 7). The LP rings disappear after those 8 minutes, when the repetitive pattern produced by the waves ends.

This picture presents some agreements with the observations. To have a glimpse of what happens below the temporal resolution element of the ZIMPOL observations (Ramelli et al. 2010), we have inspected the corresponding time evolution of the SDO photospheric images (see one snapshot in Fig. 9). We find that the link between adjacent LP rings lays between groups of photospheric magnetic elements that appear and disappear around the slit during the exposure time. This leaves a faint residue in the integrated chromospheric V/I signals: see in Fig. 9 the two weak and blurred internetwork V/I signals with opposite polarities around $x \approx 170$ arcsecs. This residual circular polarization is faint because the emergent magnetic elements, being intermittent, are not there during the whole exposure time. We think this because in our simulations the chromospheric V/I trace of similar weak magnetic elements fade away easily with exposure time too. Thus, we deduce that these small magnetic spots create field loops that reaches the low chromosphere horizontally, changing the polarity of V/I and the LP sign of the Hanle core there where the two LP rings join.

3.8. On the sign-reversals of the linear polarization

The origin of the sign reversal conforming the outer part of the LP rings is not clear because they lay in intermediate wavelengths where all plausible physical effects seem possible.

A transversal-Zeeman scenario might seem reasonable for explaining them because significant sigma Zeeman components can be produced by a magnetic field increasing rapidly downwards from the formation heights of the Hanle core. But several things point out the contrary. First, the observed LP rings have sizes compatible with the internetwork (IN) patches ($\approx 20 - 100$ arcsecs). This would imply large-scale magnetic fields acting in the IN at the level of the short-scale canopy. Namely, this would mean that large-scale organized field lines (rooted in the network, we presume) with significant chromospheric strengths ($\gtrsim 100$ G), are overlaying the IN magnetic canopy after their expansion from the network photosphere to the low IN chromosphere. This is incompatible with the current view of an IN permeated by weak short-scale fields and with the simulations. In the simulation, the slit is located very close to a network-like patch (see Fig. 1) but, even so, the transversal Zeeman signals are roughly an order of magnitude weaker than Hanle. Furthermore, as explained in Sec. 3.3, larger time integration easily weaken the sigma components even more. Finally, the presence of symmetric sign reversals aside the core in the observations is sometimes uncorrelated

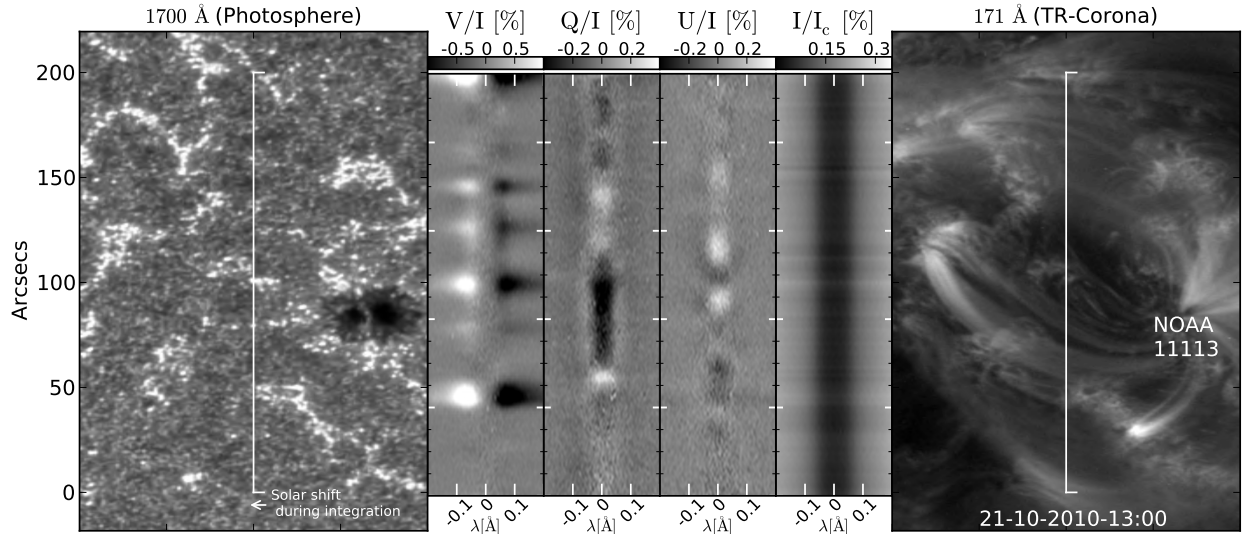


Figure 9. Zimpol@IRSOL observation in $\mu = 0.94$ (middle panels) and corresponding SDO images (lateral panels). The polarization colorbars are saturated to $\pm 1\%$ and $\pm 0.4\%$. The strongest V/I signals are always associated to the network while the weaker ones correspond to the weak photospheric magnetic elements inside the IN. Zooming the intensity one can see that there is a certain correlation between the strength of the LP rings and shorter-scale spatial intensity variations of higher contrast.

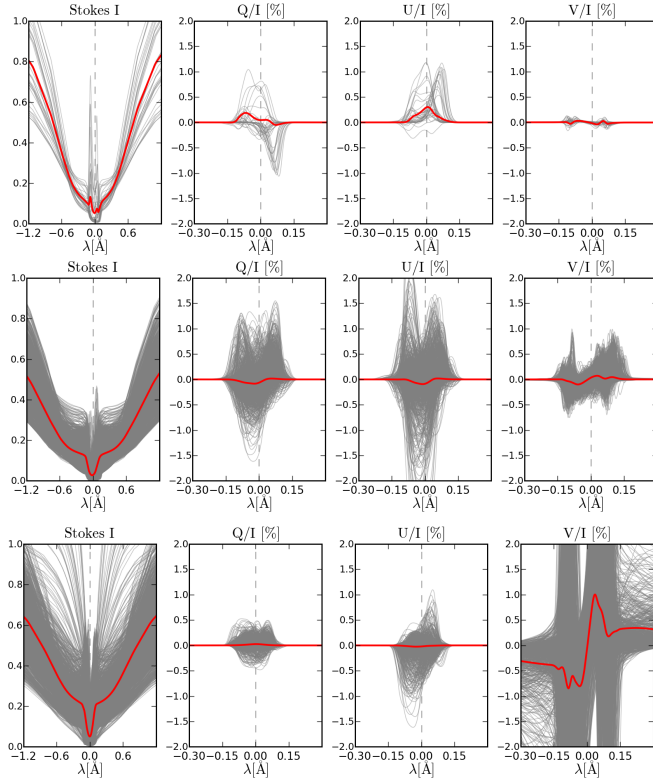


Figure 10. Effect of short and long integrations with $v_{\text{micro}} = 2 \text{ km s}^{-1}$. In gray: instantaneous Stokes profiles in a given spatio-temporal resolution element. In red: corresponding result of integrating each Stokes profiles in that bin and build the fractional quantities. Upper panels: $\Delta x = 1.4''$, $\Delta t = 20 \text{ s}$. Middle panels: $\Delta x = 1.4''$, $\Delta t = 15 \text{ min}$ in a pixel with predominantly horizontal magnetic field in the low chromosphere during the integration. Lower panels: same than before but in a pixel with more vertical and intense magnetic field.

with the kind of magnetic structures (network or IN) generating it. Hence, the transversal Zeeman effect can be ruled out.

Note that just a sign reversal in the height variation of the radiation field anisotropy cannot explain the two ob-

served near-symmetric sign reversals aside the LP core. As we expand now, there are several reasons, related to how chromospheric motions modify the anisotropy and its impact in the polarization. On one hand, there are effects controlling the sign reversals *in the resolved LP profiles*: first, the modulation of the anisotropy exerted by vertical velocity gradients can make the LP profiles antisymmetric in low-chromosphere spectral lines (second-row right panel of Fig.7 of Carlin et al, 2012.); second, the negative part of the anisotropy tends to disappear with increasing vertical gradients of the source function, e.g. with temperature gradients or in shock waves (Fig. 4 of Trujillo Bueno 2001; Carlin et al. 2013); third, when the anisotropy stratification has both negative and positive regions, the dominance of each part in the LP profiles varies significantly due the compression/expansion of the formation region around shock fronts (Fig.5.3 of Carlin et al 2013); fourth, the microturbulent velocity tends to “erase” the near-core sign reversals of LP; and fifth, the Hanle effect of a magnetic field azimuth varying with height can also produce a sign reversal in LP (see last point in Sec. 3.3), at least around disk center, where the solar-limb polarization offset is weak. The net combination of these effects varies with the spectral line and during the shocks emergence, but the theoretical trend in the chromospheric lines that we have studied is *to destroy the sign reversals in resolved LP profiles*. Thus, while anti-symmetries (only one sign reversal in the LP core) are possible and assymetries are everywhere in our simulations, it is very rare to get simultaneous sign reversals in both sides of the core. However, if on top of that we analyze the *unresolved* LP profiles resulting of such situation, we find that dynamics can mimic quasi-symmetric sign reversals due to the combination of instantaneous anisotropy-driven modulations of Hanle signals that are quasi-synchronized with Doppler shifts and integrated in space and time (Carlin & Bianda 2016). The middle panels of Fig.9 show how the instantaneous LP profiles (in gray) tend frequently to group in a sort of Zeeman $\pi - \sigma$ configuration. Hence, the same feature that was

deleted by motions in resolved signals is recreated in the integrated LP when time evolution is included. We refer to this whole situation as “dynamic Hanle” scenario.

Thus, we are left with two explanations for the symmetric sign reversals: dynamic Hanle and PRD. We try now to discriminate their relative influence by paying attention to the different location of the PRD and Hanle peaks. To show this we have applied Principal Component Analysis (PCA; e.g., Rees et al. 2000; Skumanich & López Ariste 2002; Martínez González et al. 2008) to observations of Ca I $\lambda 4227$ done with ZIMPOL at IR-SOL. We considered 450 Q/I profiles in several lines of sight ($\mu \in [0.9, 0.94]$) including profiles with PRD effects around the core. Thus, we obtained the first three PCA eigenvectors (eigenprofiles, see Fig. 11) representing 95% of the variance of the data. They are ordered (E1,E2,E3) by the amount of statistical variance that each one explains (size of the projections of the observed dataset in each eigenvector). The amplitudes of the eigenprofiles are unimportant, only shape matters.

It is known that the first PCA eigenvector (E1) typically represents the average of the data (Skumanich & López Ariste 2002), in our case mostly affected by instrumental offsets, hence unimportant. In our analysis the second eigenvector (E2) is capturing the PRD wings and separating them from the line CRD core, which is represented by the third eigenvector (E3) and dominated by Hanle and dynamics. PCA allows this separation because the contributions of dynamic Hanle and PRD are maximized at layers that behave very different (chromosphere and sub-chromospheric layers). As this happens consistently in all pixels, both physical mechanisms produce statistically uncorrelated changes in the observed profiles, so that PCA get to separate them in eigenvectors. The PRD wings of E2 have a far-wing maxima, and also a near-core minima that we assign to the sign reversals discussed here. The action of macroscopic motions appears in the asymmetry of both E2 and E3. This gives explicit evidence of the influence of macroscopic motions in observed PRD features, as advanced in Carlin & Bianda (2016). Therefore it might be important to consider the action of dynamics when studying the PRD polarization features of the second solar spectrum.

Note that the PRD minima of the eigenprofiles are broader and more separated than the minima produced by dynamic Hanle. Thus, the PCA analysis suggests that the dynamic Hanle signature is in better agreement with the width and location of the LP rings in observations. PCA does not explain the large spatial scale of the LP rings.

Inspecting Fig. 4 of Trujillo Bueno (2011), we have detected Q/I and U/I rings in quiet sun observations of another lower-chromosphere line: Ca II 8498 Å. In the same figure, the corresponding LP profiles of the $\lambda 8542$ and $\lambda 8662$, which belong to the same triplet but forms higher, exhibit slit patterns without rings. Instead, they are more like “squared” blocks along the spatial direction of the slit, most of them of single sign. This suggests that in observations of low temporal resolution the LP rings are favored by particular kinematic conditions of the lower chromosphere, and that the kinematic of upper layers somehow reduce their contrast and oval shapes. As PRD is expected to be particularly negligible in $\lambda 8498$

(Uitenbroek 1989), this supports the influence of Hanle and dynamics in the LP rings.

Our conclusion is that both dynamics and PRD contribute to the near-core sign-reversals, either because PRD itself is affected by dynamics at the very base of the chromosphere or *at least* because Hanle dynamics and PRD signatures, though forming at different heights, overlap in wavelength in each timestep.

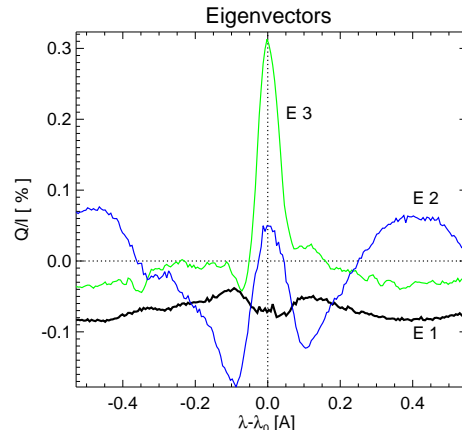


Figure 11. PCA eigenvectors for Q/I profiles taken in various LOS’s $\in \mu = [0.9, 0.96]$. Note that the PRD minima (blue) is different than the Hanle minima (green). In Fig.(14) (Appendix), this eigenprofiles are used to reconstruct some observed profiles.

3.9. Polarization time series

The study of the temporal evolution leads to significant insights about the way the solar chromosphere generates scattering polarization. First, because it exposes the effect of dynamics, so giving the possibility of discriminating them to measure chromospheric magnetic fields. Second, because it avoids the large degeneracy of integrated signals, which can clarify the origin of the anomalies found in the second solar spectrum.

Figure 12 shows spatio-temporal maps of fractional polarization at the wavelength of the absolute maximum of the profiles. This gives an estimation of the polarization structures that one may aim at observing with the S/N and spatio-temporal resolution of different ground solar facilities (see caption of the figure⁶): Irsol telescope (lower panels), Gregor (second group of panels from below) and ATST-EST class telescope (third group of panels from below). The resolution of the top panels is close to that of our calculations.

These maps support the existence of a sensitivity threshold, mentioned in the introduction, above which most of the (now hidden) scattering polarization signals should appear ‘all at once’ because the spatio-temporal scales of chromospheric dynamics is resolved.

Panels in Fig. 13 quantify and characterize the variation of the polarization amplitudes with the resolution. Note the different behavior for linear and circular polarization. Q/I and U/I are more sensitive to the temporal

⁶ The degraded maps do not result from the direct integration of the map in the top panel. In all the degraded cases, the original signals of each Stokes component were separately integrated in time, space (in x and y directions of the slit) and wavelength but preserving the whole spectral profile in each step. Then, the degraded maps were obtained by selecting the desired wavelength.

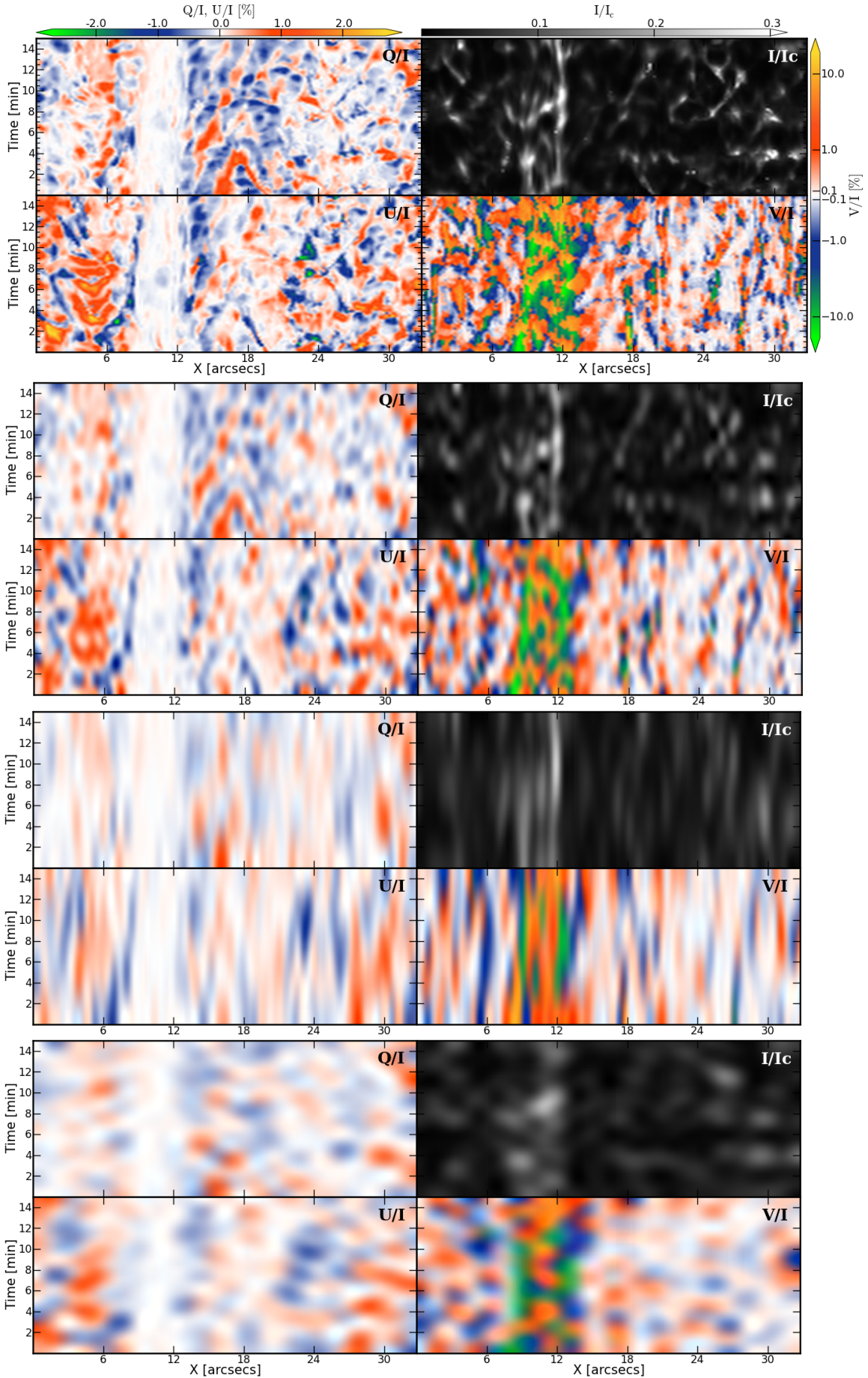


Figure 12. Time evolution of the slit Stokes vector for several resolutions. From top to bottom: $[\Delta x, \Delta t] = [0.2'', 10s]$, $[0.4'', 60s]$, $[0.4'', 180s]$, $[1.4'', 60s]$. The polarization (intensity) values were chosen in the maximum (minimum) of the spectral profile at each location. Colorbars are common, the one for V/I is logarithmic.

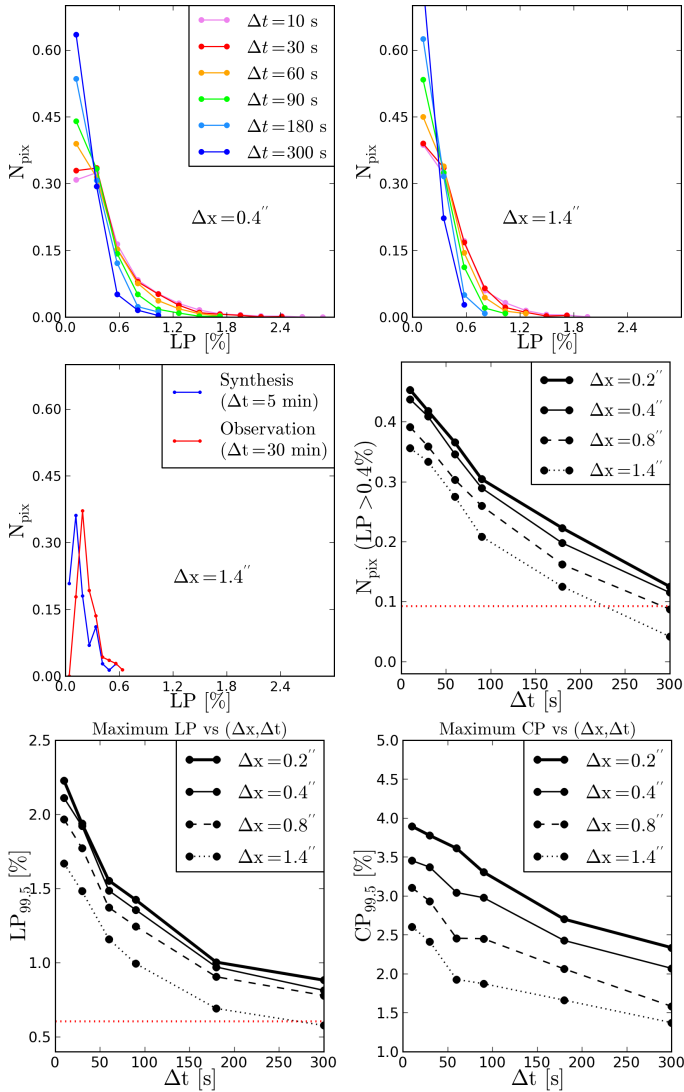


Figure 13. Upper panels: Envelopes of the normalized histograms for the total fractional LP in the given resolutions. The distributions cross in $LP \approx 0.4\%$. Left middle panel: same dark blue curve as in upper right panel (but with higher bin resolution) compared to the observation. Right middle panel: relative (to one) number of pixels (area of the normalized histograms) with $LP > 0.4\%$ versus the spatio-temporal resolution. Bottom panels: maximum fractional linear (left) and circular (right) polarization quantified as the percentile 99.5. The horizontal red lines mark the corresponding value of the LP in the observation.

evolution of the atmosphere than V/I. Independently of the spatial resolution, the first three minutes of evolution produce the largest decay of LP, while such decay is mild and almost linear in time for V/I.

4. DISCUSSION

4.1. Hanle diagnosis and polarization anomalies

Our results show how the solar scattering polarization can depend strongly on the evolution of the chromosphere. Note that despite the polarization amplitudes can decrease significantly with integration time (Fig. 13), a given short interval with favorable dynamics and magnetic fields can still restore the integrated LP to maximum values. This is so because the instantaneous signals are intrinsically large for chromospheric kinematics and

magnetic fields and because a measurement is an integration, not an average.

The spectral coherence of the polarization during the exposure time matters. Assuming a typical period of ≈ 3 minutes for the chromospheric evolution, we obtained reduced LP amplitudes of the order of $\approx 1\%$ after that time (see panel of $LP_{99.5}$ in Fig. 13). This net 1-period variation depends on the balance between the kinematic amplification of polarization due to the anisotropic Doppler brightenings (Carlin et al. 2012), the lack of spectral coherence along time (set by thermal broadening, Doppler shifts and the phase between photosphere and chromosphere waves; see Letter), and the cancellations of LP due to transfer effects along the emergent rays. If the evolution minimizes the fadings in a single-period and/or maximizes the amplifications with sufficient regularity and spectral coherence over several periods, significant signals can be measured after long exposures. The opposite situation can explain unexpectedly small signals in quiet sun locations where semiempirical models predict LP well above the detection limit (see Sec. 3.1). Thus, other spectral lines and solar regions will have their corresponding Fig. 13. We remark here the evolution of the magnetic field vector too. Its chromospheric inclination can change during the emergence of shock-driven plasma bubbles. This diminishes the LP intermittently, so reducing amplitudes after 15 minutes of integration (compare amplitudes in $12 < x < 20$ Mm and $x > 20$ Mm in right-most panel of Fig. 7). Through these mechanisms, dynamics increases the range of possible LP amplitudes.

This means that the systematic overlooking of kinematics and time evolution has falsified the previous interpretations of chromospheric Hanle polarization. Curiously, such “static” approach appeals because both the lack of resolution in the observations and the lack of kinematics in scattering calculations compensate each other within the uncertainties that could be explained with Hanle depolarization. Indeed, the maximum observed polarization amplitudes of several spectral lines agree with the maximum theoretical amplitudes given by semiempirical, hence static, models of the chromosphere. This assertion is surprisingly precise for the Ca I 4227 Å line because the maximum disk-center total fractional LP amplitudes for any $B < 150$ G are always between 0.4-0.5% (see Sec. 3.1), very close to the observed maximum of 0.6%. In cases without such an agreement, the differences have been typically explained assuming Hanle-depolarizing magnetic field inclinations, excluding the suspicious and challenging anomalous excesses of line-core polarization in certain chromospheric lines (Landi Degl’Innocenti 1998; Stenflo et al. 2000). Our results point out that such difficult cases are precisely showing the limitations of the static approach. The mere presence of shock waves is sufficient for obtaining *instantaneous* polarization enhancements of up to one order of magnitude with respect to calculations in static or to temporally unresolved observations. Joining this with a coherent (constructive) dynamics during long exposures, it is possible to explain the excesses of polarization in the second solar spectrum. This favorable situation should be more frequent at the limb, where the anomalous signals appear. There, the height-dependent radiation anisotropy tends to be mapped always in its

positive part and the LOS Doppler shifts produced by the emergent waves are minimized, so the spectral LP enhancements are more easily coherent, hence reinforced.

The analysis and interpretation of the second solar spectrum requires a new paradigm in which the origin of the scattering signals (the symphony) have to be explained as the result of an atomic system (the instrument) instantaneously reacting to the solar atmosphere (the playing musician). A key remark is that *the observed solar polarization is strongly determined by the temporal, geometrical and spectral variation of the illumination that the scatterers receive*, which is ultimately controlled by relative motions around them. Thus, polarization signals can have both large variability and degeneracy, hence we need a way to systematically expose, group or constrain this broad range of possibilities. Can we do this with semiempirical models? Are MHD models enough?

4.2. About semiempirical models and heatings

The fact that semi-empirical models do not always explain the observed polarization has been noted by several works (e.g., Smitha et al. 2014; Supriya et al. 2014), though the reasons were unclear. The dynamic effects affecting the scattering polarization cannot be reproduced by semi-empirical models because they do not depend on time and treat macroscopic kinematics as ad-hoc microturbulent velocity. Dynamic effects cannot be modelled by macroturbulence neither, because it just changes the shape of the emergent signals but not the polarization properties of the media, similarly to what happens with the velocity-free approximation (Carlin et al. 2013).

The effect of dynamics is more important as we increase resolution. The microturbulent motions parameterized in semi-empirical models act as effective Doppler shifts in the profiles when considering resolved observations or MHD simulations. In other words, the dynamic ratio (Doppler velocity in Doppler units),

$$\xi(s) = \frac{v_{\text{res}}}{v_{\text{unres}}} = \frac{v_{\bar{\Omega}}}{\sqrt{v_{\text{thermal}}^2 + v_{\text{micro}}^2}},$$

which controls the modulation of anisotropy and LP, increases with resolution because the microturbulent velocity (v_{micro}) passes to be accounted in the numerator as resolved macroscopic velocity ($v_{\text{res}}=v_{\bar{\Omega}}$) along the optical path “s” of each ray $\bar{\Omega}$. Note that unresolved velocities are both thermal and microturbulent, but only the latter gives a pool of motions that can act as effective Doppler shifts with increased resolution.

Larger ξ usually implies larger instantaneous LP amplifications but, depending on the evolution of the thermal broadening (heatings) and kinematics, it can also ease cancellations after temporal integrations due to signs mixing and spectral incoherence. Thus, microturbulence not only compensates broadening (lack of heating), it is also encoded in the LP amplitudes (Sec. 3.5). This happens through changes in the radiation field anisotropy perceived by the scatterer but also in the amount of atomic population that is pumped to the upper level. For instance, consider a scatterer in the coolest solar layers. A broader absorption profile (larger microturbulence) allows it to capture more pumping light (even without motions) that otherwise would be screened by the even broader profiles sandwiching the region of the tem-

perature minimum. In summary, cooler plasma means scattering polarization more sensitive to kinematics and heatings. Therefore, the shape, width and amplitude of polarization profiles are a strong test/constrain for the models, even with time integration. This and the current lack of understanding on the distribution of solar chromospheric heatings mean that the choice of microturbulence in calculations of polarization has larger relevance than usually believed.

The fact that the chromospheric temperatures in the MHD models are cooler than in the sun (Leenaarts et al. 2009) motivated the MHD simulations with higher resolutions considered here. But larger broadenings are still needed. Extra broadening might come from further-increased resolutions in the MHD calculation. However we think that this will not improve the fit with the observations because the LP profiles would be then narrower and with larger velocities, hence more sensitive to the distribution of motions and prone to loose spectral coherence. This would bring a more efficient cancellation of LP (as in our results without microturbulence), worsening the agreement with observations. Thus, larger temperatures should come from purely thermal sources (v_{thermal}), not from unresolved motions.

Solving the chromospheric and coronal heating problems requires to understand how the heating sources are distributed in space and time in the solar plasma. Remarkably this problem could be studied using spectral lines as the $\lambda 4227$, whose line core form in the lower chromosphere. There, with minimum temperatures, small variations in temperature become more notable than at the transition region or corona, at least in regard to scattering polarization.

4.3. Three-dimensional effects

Though in some areas of the disk center the calculations in 1.5D and in 3D seem to give similar results (Štěpán & Trujillo Bueno 2016), the 1.5D approximation does not contain the effect of horizontal velocity gradients nor of horizontal inhomogeneities. The goal of the following discussion is to point out some subtleties related with the relative strength of each polarizing effect.

The first one is that three-dimensional effects in the solar polarization may be controlled by dynamics instead of by “plasma inhomogeneities” (spatial lumps of temperature and density). The net pumping radiation at a given scattering point is affected by two contributions: one given by the anisotropic radiation coming from other points in an inhomogeneous *but static* atmosphere; and a latter one modulating the former when velocities act in the radiative transfer connecting each point with the scatterer. Namely, differential velocities all over the formation region (seen by the scatterer) create opacity-changing Doppler shifts along the pumping rays that change the radiation created by the inhomogeneities. In particular, the distribution of horizontal kinematics is, as we develop now, essential for understanding 3D effects because it easily sculpts the effective horizontal radiation field.

The second idea follows. What happens in an atmosphere without preferred horizontal directions? Here the light converging horizontally in each plasma element is affected, at each point of a long optical path, by *randomly-organized horizontal velocity gradi-*

ents. This can approximate a net cancellation of the positive and negative azimuth-dependent radiation field components⁷. In this way their contribution to the atomic polarization can be largely exceeded by the combined contributions of: 1) the ever-present and comparatively strong vertical gradients driven by shock waves and gravity, which are geometrically “organized” ; and 2) the limb brightening/darkening. The 1.5D approximation considers both, hence if horizontal motions had such an isotropizing effect, the fractional LP in 1.5D would approach the 3D results in larger quiet sun areas. In this “dynamic” physical limit, disorganized horizontal velocity gradients minimize the azimuthal anisotropy of the radiation created by inhomogeneities. Thus, though being an opposite situation to that of a 1.5D atmosphere (limit without horizontal gradients/inhomogeneities), both situations let atomic polarization be driven by the vertical stratification of plasma properties. The solar atmosphere is somewhere between these two conceptual limits.

The last subtlety to mention has to do with the fact that three-dimensional solar models are of relatively recent apparition. This implies that their chromospheric horizontal velocity fields lacks of observational feedback and should be expected to fail at reproducing the limb intensity of chromospheric lines. Contrarily to the “observationally-tuned” vertical velocities (Carlsson & Stein 1997), which are basically guided by shock waves and gravity, the less-investigated horizontal velocity (gradients) should furthermore depend on the distribution and scales of the magnetic fields in the models. Adding this to the indirect sensitivity that the LP has on temperature through kinematics (recall Sec. 4.2), we conclude that the differences between 3D and 1.5D calculations might be quiet influenced by ingredients of the models that require improvement.

We show the relevance of these ideas commenting on two of the few papers existing on this topic. The key is that the influence of the 3D radiation field on the Hanle polarization has been posed since the beginning in terms of inhomogeneities, and not in terms of velocity gradients. The initial conclusions to this regard were obtained by Manso Sainz & Trujillo Bueno (2011) with an analytical/numerical study approaching the problem in static regime. In more recent numerical studies the action of 3D velocities in the polarization is included, but the contributions of vertical and horizontal velocity gradients are not separated. As the effects of horizontal velocity gradients and inhomogeneities are in turn blended, it is also unknown which are their relative contributions to the differences between 1.5D and 3D calculations. Consider for instance Fig. 3 of Štěpán & Trujillo Bueno (2016), which points out that the Hanle effect at disk center *tends* to depolarize when is accompanied by other symmetry breaking effect, as happens in the well-known case of the solar limb. The figure also confirms that macroscopic motions are yet an efficient polarizing source for the spectral line considered (as known from 1D simulations of the Ca II IR triplet, Carlin et al. 2013). However, it is unknown whether the polarization introduced by velocity in that

figure is due to the horizontal or to the vertical velocity gradients already considered in 1D calculations. This matters not only for comparing with 1D calculations, but also because horizontal velocity gradients can potentially compensate and exceed the polarization created by horizontal inhomogeneities (as explained in previous paragraphs). Thus, the dominant symmetry breaking and polarizing effect at disk center could not be the inhomogeneities, as always affirmed, but the horizontal velocity gradients. Hence, we think that is key to quantify the *sensitivity* of such results to the *model horizontal distribution of velocity gradients*, which also can help to detach the conclusions from the eventual lack of realism in them. Finally, it is also to be noted that when those radiative transfer simulations do not add microturbulent velocity, they use the temperature distribution of MHD models that are known to represent a chromosphere cooler than the solar one. Thus, as temperature influences significantly the effect of the velocities in the LP (see Sec. 4.2 of the present paper), the relative strength of the polarizing effects discussed here might change accordingly.

In summary, horizontal velocity gradients compete with other physical mechanisms, such as inhomogeneities and Hanle effect, for polarizing and depolarizing the light, hence we need to explicitly quantify whether they are effectively relevant for inferring magnetic fields with the Hanle effect. We need to find theoretical and observational methods for discriminating the Hanle effect. Temporal evolution might help to this aim, which motivated the present paper. Other possibility is to explore the concept of Hanle PILs (Carlin & Asensio Ramos 2015): as in saturation the Hanle effect always nullify the polarization for particular magnetic field orientations, it creates an ever-present spatial fingerprint of the magnetic field topology in polarization maps.

5. CONCLUSIONS

Considering the radiation-MHD simulation of Carlsson et al. (2016), we have simulated the temporal evolution of the spectral line polarization of the Ca I 4227 Å line in forward scattering, including the Hanle and Zeeman effects.

We find that the large forward-scattering amplitudes of the $\lambda 4227$ line are accentuated by its formation region, which is in the temperature minimum and close to the short-scale IN canopy of horizontal magnetic fields. This maximizes the impact of macroscopic motions in the LP and the Hanle effect respectively. Without the amplification of polarization produced by dynamics, the effect of temporal integration in current observations would make impossible to detect the scattering polarization signals of this line in the disk center.

At least the strong spectral lines forming in the lower chromosphere are expected to show the largest sensitivity to kinematics and atmospheric heatings in linear polarization. Hence they offer a possible test bench for understanding the distribution of chromospheric heatings through the scattering polarization. However, there where the evolution of dynamics has no sufficient spectral and temporal coherence the cancellation of signals can make them undetectable. Thus, the evolution of dynamics might be key for explaining the polarization profiles and perhaps the eventual absence of polarization in large areas.

⁷ This azimuthal isotropization of the field should be more effective the larger the horizontal extension of the formation region and the less organized are the horizontal velocity gradients.

Our calculations indicate that the measurement of polarization time series with exposure times below a minute should be of great help for Hanle diagnosis. In the Ca I 4227 Å line, spatial resolutions as large as 0.4'' seem enough to detect the Hanle structures of the chromosphere as soon as time resolution is achieved.

The discrimination of Hanle, Zeeman and PRD effects in the generation of LP rings could not be completely clarified here but the situation was exposed in better detail presenting several clues that can guide deeper investigations. The near-core region of the LP profiles is challenging because all possible effects overlap.

It seems necessary to revisit those studies of the second

solar spectrum where a formal comparison between theory and observations has been done without accounting for the effect of kinematics and time evolution.

Dedicated to Prof. Egidio Landi Degl'innocenti, who passed away during the publication of this paper. We thank J. Leenaarts and M. Carlsson for providing the atmospheric models and for valuable comments and discussions. We thank J. Leenaarts for a careful reading of the manuscript that helped to improve the text, and J. Stenflo and O. Steiner for their feedback and discussions. This work was financed by the SERI project C12.0084 (COST action MP1104) and by the Swiss National Science Foundation project 200021_163405.

APPENDIX

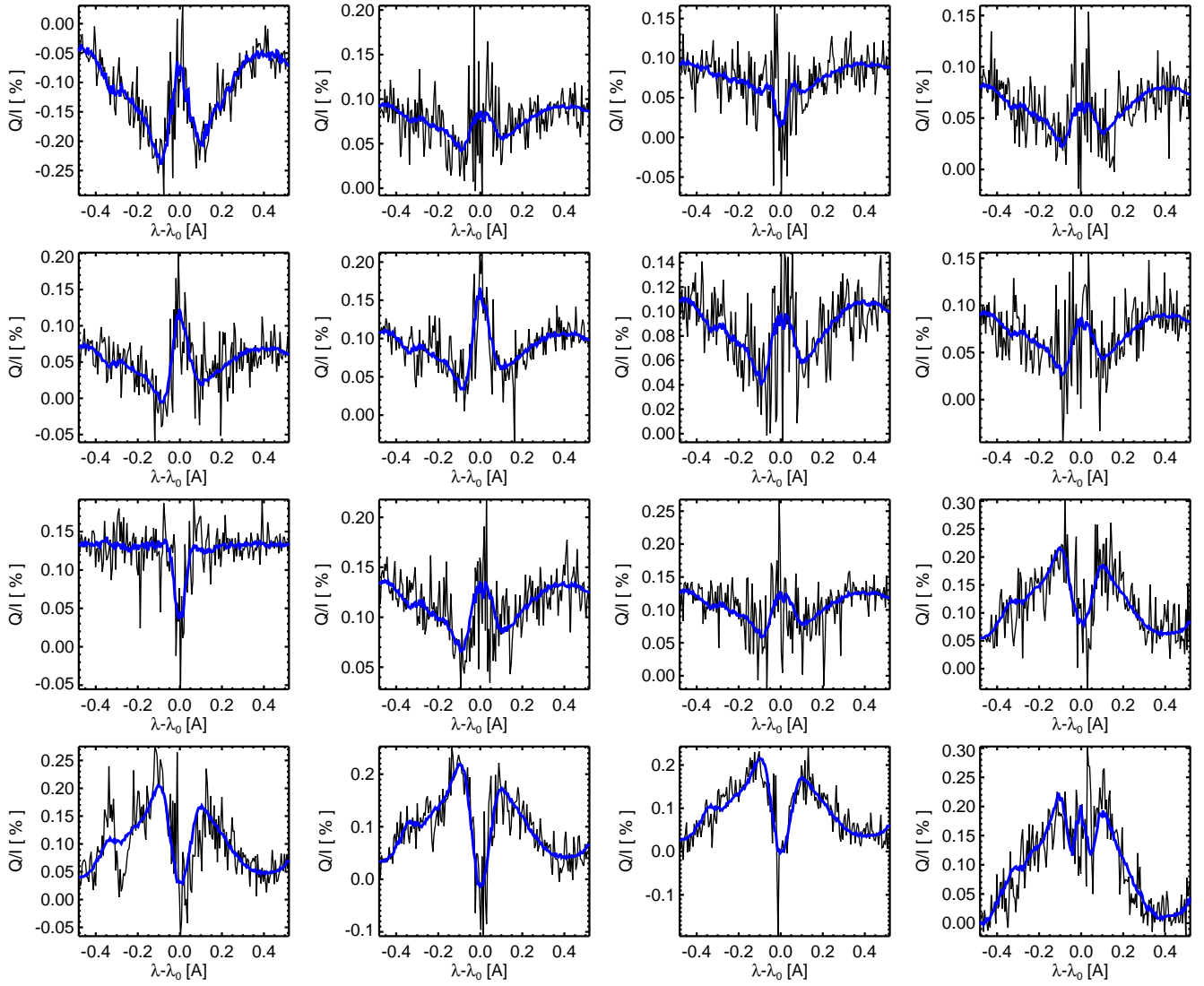


Figure 14. Example of some random observed profiles of Ca I 4227 Å (black line) that have been reconstructed (blue line) using the first three PCA eigenvectors of our database.

REFERENCES

- Anusha, L. S., Nagendra, K. N., Bianda, M., Stenflo, J. O., Holzreuter, R., Sampoorna, M., Frisch, H., Ramelli, R., & Smitha, H. N. 2011, *ApJ*, 737, 95

- Anusha, L. S., Nagendra, K. N., Stenflo, J. O., Bianda, M., Sampoorna, M., Frisch, H., Holzreuter, R., & Ramelli, R. 2010, *ApJ*, 718, 988
- Bianda, M., Ramelli, R., Anusha, L. S., Stenflo, J. O., Nagendra, K. N., Holzreuter, R., Sampoorna, M., Frisch, H., & Smitha, H. N. 2011, *A&A*, 530, L13
- Bianda, M., Solanki, S. K., & Stenflo, J. O. 1998, *A&A*, 331, 760
- Brückner, G. 1963, *Z. Astrophys.*, 58
- Carlin, E. S. 2015, in *IAU Symposium*, Vol. 305, *Polarimetry*, ed. K. N. Nagendra, S. Bagnulo, R. Centeno, & M. Jesús Martínez González, 146–153
- Carlin, E. S. 2016, arXiv:1612.05091v2 [astro-ph.SR], SPW 8 proceedings
- Carlin, E. S., & Asensio Ramos, A. 2015, *ApJ*, 801, 16
- Carlin, E. S., Asensio Ramos, A., & Trujillo Bueno, J. 2013, *ApJ*, 764, 40
- Carlin, E. S., & Bianda, M. 2016, *ApJ*, 831, L5
- Carlin, E. S., Manso Sainz, R., Asensio Ramos, A., & Trujillo Bueno, J. 2012, *ApJ*, 751, 5
- Carlsson, M., Hansteen, V. H., Gudiksen, B. V., Leenaarts, J., & De Pontieu, B. 2016, *A&A*, 585, A4
- Carlsson, M., & Stein, R. F. 1997, *ApJ*, 481, 500
- Collados, M., Bettonvil, F., Cavaller, L., Ermolli, I., Gelly, B., Pérez, H., A. -N., Soltan, D., Volkmer, R., & EST Team. 2013, in *Highlights of Spanish Astrophysics VII*, 808–819
- Dumont, S., Pecker, J.-C., & Omont, A. 1973, *Sol. Phys.*, 28, 271
- Dumont, S., Pecker, J. C., Omont, A., & Rees, D. 1977, *A&A*, 54, 675
- Faurobert-Scholl, M. 1992, *A&A*, 258, 521
- Fontenla, J. M., Avrett, E. H., & Loeser, R. 1993, *ApJ*, 406, 319
- Goodman, M. L. 1996, *ApJ*, 463, 784
- Gudiksen, B. V., Carlsson, M., Hansteen, V. H., Hayek, W., Leenaarts, J., & Martínez-Sykora, J. 2011, *A&A*, 531, A154
- Holzreuter, R., Fluri, D. M., & Stenflo, J. O. 2005, *A&A*, 434, 713
- Lamb, F. K., & Ter Haar, D. 1971, *Physics Reports*, 2, 253
- Landi Degl’Innocenti, E. 1998, *Nature*, 392, 256
- Landi Degl’Innocenti, E., & Landolfi, M. 2004, *Polarization in Spectral Lines* (Kluwer Academic Publishers)
- Leenaarts, J., Carlsson, M., Hansteen, V., & Rouppe van der Voort, L. 2009, *ApJ*, 694, L128
- Leenaarts, J., Pereira, T., & Uitenbroek, H. 2012, *A&A*, 543, A109
- Lites, B. W. 1974, *A&A*, 30, 297
- Manso Sainz, R., & Trujillo Bueno, J. 2011, *ApJ*, 743, 12
- Martínez González, M. J., Asensio Ramos, A., Carroll, T. A., Kopf, M., Ramírez Vélez, J. C., & Semel, M. 2008, *A&A*, 486, 637
- Pereira, T. M. D., & Uitenbroek, H. 2015, *A&A*, 574, A3
- Ramelli, R., Balemi, S., Bianda, M., Defilippis, I., Gamma, L., Hagenbuch, S., Rogantini, M., Steiner, P., & Stenflo, J. O. 2010, *SPIE*, 77351Y
- Rees, D. E., López Ariste, A., Thatcher, J., & Semel, M. 2000, *A&A*, 355, 759
- Rimmele, T., Berger, T., McMullin, J., Keil, S., Goode, P., Knoelker, M., Kuhn, J., Rosner, R., Casini, R., Lin, H., Woeger, F., von der Luehe, O., Tritschler, A., & Atst Team. 2013, in *EGU General Assembly Conference Abstracts*, Vol. 15, *EGU General Assembly Conference Abstracts*, 6305
- Sampoorna, M., Stenflo, J. O., Nagendra, K. N., Bianda, M., Ramelli, R., & Anusha, L. S. 2009, *ApJ*, 699, 1650
- Skumanich, A., & López Ariste, A. 2002, *ApJ*, 570, 379
- Smitha, H. N., Nagendra, K. N., Stenflo, J. O., Bianda, M., & Ramelli, R. 2014, *ApJ*, 794, 30
- Stenflo, J. O. 1974, *Sol. Phys.*, 37, 31
- Stenflo, J. O., Keller, C. U., & Gandorfer, A. 2000, *A&A*, 355, 789
- Supriya, H. D., Smitha, H. N., Nagendra, K. N., Stenflo, J. O., Bianda, M., Ramelli, R., Ravindra, B., & Anusha, L. S. 2014, *ApJ*, 793, 42
- Tichý, A., Štěpán, J., Trujillo Bueno, J., & Kubát, J. 2015, in *IAU Symposium*, Vol. 305, *Polarimetry*, ed. K. N. Nagendra, S. Bagnulo, R. Centeno, & M. Jesús Martínez González, 401–406
- Trujillo Bueno, J. 2001, in *Astronomical Society of the Pacific Conference Series*, Vol. 236, *Advanced Solar Polarimetry – Theory, Observation, and Instrumentation*, ed. M. Sigwarth, 161
- Trujillo Bueno, J. 2011, in *Astronomical Society of the Pacific Conference Series*, Vol. 437, *Solar Polarization 6*, ed. J. R. Kuhn, D. M. Harrington, H. Lin, S. V. Berdyugina, J. Trujillo-Bueno, S. L. Keil, & T. Rimmele, 83
- Uitenbroek, H. 1989, *A&A*, 213, 360
- . 2001, *ApJ*, 557, 389
- Štěpán, J., & Trujillo Bueno, J. 2016, *ApJ*, 826, L10
- Štěpán, J., Trujillo Bueno, J., Leenaarts, J., & Carlsson, M. 2015, *ApJ*, 803, 65